Unraveling the response of the actin cortex to electric pulses in vesicles

D. L. Perrier, A. Vahid, V. Kathavi, L. Stam, L. Rems, Y. Mulla, G. H. Koenderink, M. T. Kreutzer, P. E. Boukany

Abstract

The plasma membrane is essential for maintaining the integrity of living cells. Its shape and mechanical properties are regulated by a subjacently attached interconnected network of actin filaments, known as the "actin cortex". The actin cortex is a major factor influencing the mechanical response of the cell to external physical cues. In this study, using giant unilamellar vesicles (GUVs) as a model system, we investigate the role of the actin cortex during the application of electric pulses that induce electroporation or electropermeabilization. We demonstrate that the presence of an actin cortex inhibits the formation of macropores in the electroporated GUVs and slows down the resealing process of the permeabilized membrane. We further analyze the stability of the actin cortex inside the GUVs exposed to high electric pulses. We find disruption of the actin cortex that is likely due to the electrophoretic forces acting on the actin filaments during the permeabilization of the GUVs. Our findings also reveal that the current simplified experimental models of cells need to be endowed with an actin cortex in order to more closely mimic the complex nature of cellular membranes.

1 Introduction

The plasma membrane is a selective barrier that separates the intracellular environment from the cell exterior and regulates the transport of molecules of different sizes in or out of the cell. The membrane consists of a lipid bilayer with numerous anchored and embedded inclusions, providing the membrane with both fluidic and elastic properties; additionaly, an inter-connected network of actin filaments, called the actin cortex, lies immediately underneath the plasma membrane. The cortical skeleton is strongly bound to the lipid bilayer via diverse linkers, maintaining the global shape of the cell (1–3), and controlling the lateral organization of the plasma membrane (4, 5). The bi-directional interplay between the membrane and actin cortex strongly influences any mechanical response of the cell to external stimuli during diverse biological processes, ranging from cell migration and differentiation to cell division (6).

The cortical network also plays an essential role in the electroporation, also referred to as electropermeabilization, of cells, the mechanisms by which the delivery of a wide range of molecules ranging from small molecules such as drugs to large molecules such as DNA into the cell is achieved. Applying direct current (DC) electric pulses to a cell builds up an induced transmembrane voltage, which can permeabilize the cell membrane above a critical transmembrane voltage ($\sim$ 0.2 - 1 V) (7, 8). The kinetics of the electroporation mechanisms in cells appears to consist of five consecutive steps: (i) nucleation of defects in the membrane, (ii) expansion of these defects, (iii) stabilization of the permeabilized state, (iv) resealing of the permeated membrane, (v) the long-term recovery of some structural changes in the membrane, also called the "memory" of the cell, while the membrane is already resealed (8). It has been shown that cells can remain permeabilized from minutes up to hours after pulsation (9–11). This long resealing process is considerably slower than that observed for bare lipid bilayers (less than one second) (12–14). Additionally, it was reported that the permeabilized area in cells after electro-fusion does not diffuse laterally (15). Based on this evidence, it has been suggested that the actin cortex is involved in the electroporation mechanism (16, 17). The physical properties of such transient permeated lipid structures and the associated intracellular components are the most important factors that enable a successful delivery to the cells (8, 18–20). Until now, a complete understanding of the effects of the actin cortex on electroporation of a lipid bilayer is lacking.

There have been several studies on the role of the cytoskeleton during electroporation of living cells (21–30). In these studies, the actin filaments were manipulated either by drugs that cause disruption (21–23, 27) or stabilization (24) or by genetic engineering (25) of the actin cortex. The permeabilization of the cells was measured in terms of the uptake or release of tracer molecules, like Trypan Blue and Propidium Iodide (21–28). Depolymerization of the actin in chinese hamster ovary (CHO) cells and human erythrocytes leads to acceleration of the post-pulse membrane resealing, while it does not considerably affect the initial steps in the permeabilization process which are responsible for bringing the membrane into the permeable state (21, 22). Recently, nanosecond pulses have gained attention due to their ability to permeabilize intracellular membranes (31). Disruption of the actin cortex in CHO cells appears to make the cells more susceptible to nanosecond electroporation (26). Moreover,

nanosecond electroporation was found to be more damaging to non-adherent cultures such as Jurkat cells than adherent cell cultures such as HeLa cells, possible because of the less extensive cytoskeleton network of the former (28). In addition, some biological processes, like apoptosis (the self-killing process of the cell) and necrosis, have been triggered by nanosecond pulses (27, 29), which could involve the pulse-mediated disruption of the actin cytoskeleton (23, 30).

The studies discussed above illustrate how challenging it is to decouple the mechanical interaction between actin filaments and the membrane from other biological processes involving actin, such as apoptosis and necrosis, and to manipulate the cytoskeleton of a living cells without side effects, like cell death. Therefore, simplified cell models like planar lipid bilayer models (32–34) and giant unilamellar vesicles (GUVs) (35–37) have been utilized to study the fundamental mechanisms of pore formation during electroporation. The process of pore formation involves a balance between membrane tension and edge tension. During the pulse, the electric field imposes a Maxwell stress on the membrane, similar to lateral tension (38, 39) This membrane tension of the lipid bilayer increases, driving the pore formation in order to release it (40, 41). After the pore formation, the growth of the pore can be regulated by the intensity and the duration of electric pulses (11, 42). On the contrary, the edge tension confers an energy penalty for making a pore in the lipid bilayer and counteracts the pore growth. After the electric pulse, this edge tension governs the resealing of the pore (42, 43). Studies on GUVs have revealed the presence of micrometer sized pores (referred to as macro-pores) during electroporation (12, 41, 44–46). The membrane resealing time of these pores is typically in the order of 10 ms (41), as opposed to several minutes or even hours in living cells. It has been shown that the dynamics of these pores can be modified by adjusting the edge tension of the lipid bilayer, e.g. by adding cholesterol to increase the edge tension (40, 47). Moreover, gel-phase lipids have been shown to prevent the formation of macropores due to high surface viscosity (48, 49). From these studies, it can be concluded that the membrane components are crucial for the dynamics of electropermeabilization in cells.

Although the same physics governs the competition between the membrane tension and edge tension during pore formation, GUVs and living cells exhibit drastically different pores or permeabilized membranes. The pores formed in GUVs due to pulse application are in the micrometer range, and reseal within tens of miliseconds. By contrast, the electropores (or permeated membrane) in living cells were reported to be in the order of few nanometers (11, 50, 51) and express a slow resealing process which takes minutes up to hours (50, 52, 53), suggesting that the permeabilization dynamics are influenced by an interplay between the lipid bilayer and the intracellular structures, in addition to other lipid-associated interactions (16, 22).

In this research, we focus on the role of the actin cortex during electroporation of the membrane in order to understand the discrepancy between model membranes and the plasma membrane. To isolate the mechanical role of the actin, we have used a bottom-up approach where the GUVs are supported by an actin cortex. We have used a high-speed imaging technique to reveal the pore formation and resealing in response to controlled electric pulses

for GUVs, with and without an encapsulated actin cortex. Additionally, we use confocal imaging to investigate the structural stability of the encapsulated actin cortex in the electric field.

2 Materials and Methods

2.1 Preparation of the GUVs

The GUVs (with and without actin filaments) were prepared by electroswelling, based on a procedure utilized by Schäfer et al. (54). The following membrane composition was used for the bright field experiments: 95 mol % 1,2-dioleoyl-*sn*-glycero-3-phospholine (DOPC) and 5 mol % Ca^{2+}-ionophore. For the confocal experiments, the membrane was fluorescently labelled using the following membrane composition: 94.5 mol % DOPC, 5 mol % Ca^{2+}-ionophore and 0.5 mol % 1,2-dioleoyl-*sn*-glycero-3-phosphoethanolamine-N-(lissamine rhodamine B sulfonyl) (ammonium salt) (DOPE-RhoB, ex/em 560 nm/583 nm). The lipids were purchased from Avanti Polar Lipids, Inc and the Ca^{2+}-ionophore from Sigma Aldrich, and stored at -20 °C. All membrane components were dissolved separately in chloroform at a concentration of 1 mg/ml, stored under nitrogen at -20 °C, and mixed prior to the experiments. 10 μl of lipid mixture was deposited on the conductive face of two Indium Tin Oxide (ITO) slides (purchased from Sigma Aldrich) and left under vacuum for more than 2 hours. Afterwards, the ITO slides were inserted in the teflon swelling chamber with the conductive sides facing each other, spaced 1.5 mm apart. 335.6 μL swelling buffer (pH of $\sim$ 8) was inserted in between the ITO slides, consisting of 200 mM sucrose, 2 mM Tris-HCl (Thermo Fischer), 0.17 mM Adenosine 5'-triphosphate disodium salt hydrate (Na_2ATP) and 0.21 mM dithiothreitol (DTT) (both purchased from Sigma Aldrich). In the case of the GUVs with encapsulated filaments, actin monomers from rabbit muscle (Thermo Fischer), purchased as 1 mg of lyophilised powder, was dissolved in 2 mM Tris-HCl (pH 8.0) to get a stock solution of 2 mg/ml and stored at -80 °C. For visualization of the filaments, fluorescently labeled actin monomers with Alexa488 (Thermo Fischer, ex/em 495 nm/519 nm) was purchased as a solution with a concentration in the range of $3 - 5$ mg/ml in a buffer (5 mM Tris (pH 8.1), 0.2 mM DTT, 0.2 mM $CaCl_2$, and 0.2 mM ATP) containing 10% (w/v) sucrose. A solution of 7 μM actin monomers, of which 0.5 μM fluorescently labeled, was added to the swelling buffer. An alternating current (AC) was applied at 70 Hz, 2.4 V for 3 hours at room temperature (around 20 °C), using the Agilent 33220A 20 MHz Function / Arbitrary Waveform Generator.

2.2 Polymerization and binding of actin to the membrane

The polymerization of the actin filaments and their attachment to the membrane were induced by adding Mg^{2+} ions (54), as shown in Figure 1B. The GUV solution obtained by electroswelling was diluted with 1.3 mL glucose buffer of 200 mM glucose and 2mM Tris-HCl (pH of $\sim$ 8) in order to dilute the actin monomer concentration and the sucrose concentra-

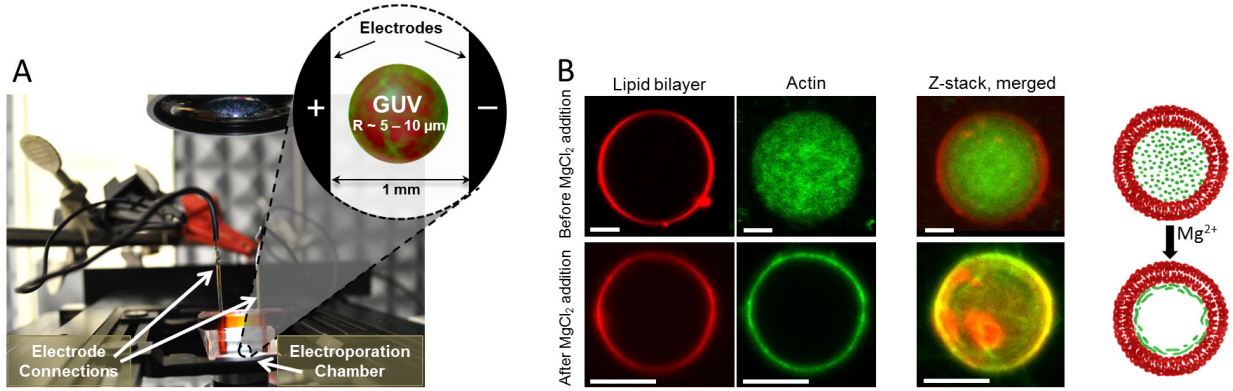

Figure 1: (A) Photograph of the electroporation setup, with a schematic of the GUV in between the electrodes shown in the inset, not drawn to scale. (B) Confocal fluorescence microscopy images of a GUV (red signal, ex/em 560 nm/583 nm) before and after the addition of 19 mM $MgCl_2$, showing that actin polymerizes and accumulates underneath the lipid bilayer membrane (green signal, ex/em 495 nm/519 nm).

tion on the outside of the GUVs. 163 μL of 67.3 mM $MgCl_2$ solution (pH of $\sim$ 8.5) was then added to increase the $MgCl_2$ concentration to 6 mM. Subsequently, due to the presence of the Ca^{2+}-ionophore in the membrane, the Mg^{2+} ions are transported into the GUVs to initiate polymerization and bind the actin filaments to the membrane as a cortex, left overnight at room temperature. Prior to the electroporation experiments, the $MgCl_2$ concentration in the outer solution was increased to 19 mM to ensure a cortex at the membrane for all GUVs. This increase in the $MgCl_2$ concentration to 19 mM after equilibrating the GUVs at 6 mM overnight has led to the most consistent result with a large majority of GUVs containing an actin cortex (> 90 %). Since the ion concentration has a large impact on the response of the GUVs to electric pulses (55), we fixed the concentration of $MgCl_2$ at 19 mM.

2.3 Electroporation setup combined with high speed imaging

To image the dynamics of the membrane during an electric pulse, the GUVs were visualized by an inverted microscope (Zeiss Axio Observer.Z1) equipped with a Phantom v9.1 high-speed camera ($10\,000 - 15\,000$ frames per second, fps, Vision Research Inc.), using a 40x oil immersion objective (Ph3, Plan-Neofluar, 40x/1.30), providing a pixel size of 0.3 μm. Prior to the experiments, the imaging chamber was treated with 5 g/L Bovine Serum Albumin (BSA) solution (purchased from Sigma Aldrich) for 20 minutes, to avoid rupture of the GUVs when interacting with the glass bottom of the chamber. Custom made stainless-steel 20 mm-long electrodes with 1 mm distance were submerged in 1 mL glucose buffer with 412.4 μL $MgCl_2$ and 33 μL of GUV solution was added by carefully pipetting the GUV-solution in between the electrodes using a cut-off pipette tip (Figure 1A). We selected the actin-encapsulated GUVs based on the fluorescence signal of the actin, to ensure that the filaments were organized along the GUV membrane as a cortex, as shown in Figure 1B.

During the dynamics experiments, consecutive increasing 500 μs pulses were applied. The electric pulses induce a transmembrane voltage as follows (56):

$$\Psi_{\mathrm{m}} = 1.5\mathrm{RE}\left(1 - \exp(-\mathrm{t}/\tau)\right), \tag{1}$$

where R, E and t indicate the radius of the GUV, the applied electric field strength and the duration of the pulse, respectively. τ is the charging time of the membrane given by

$$\tau \approx \mathrm{RC_m}(1/\lambda_{\mathrm{e}} + 1/\lambda_{\mathrm{i}}), \tag{2}$$

where $\mathrm{C_m}$, λ_{e} and λ_{i} are the membrane capacitance, and the internal and external solution conductivity, respectively. In our experiments the pulses were chosen such that the induced transmembrane voltage started from about 1 V, with approximately 1 minute interval between the pulses to minimize the effect of the former pulse. The sucrose-filled GUVs with glucose solution on the outside assure sufficient optical contrast to image the GUVs in bright field, and indicate permeabilisation of the membrane by a contrast loss. Consecutive increasing pulses were applied until a complete contrast loss of the GUVs was observed.

2.4 Electroporation chamber combined with confocal imaging

The response of the actin cortex to the electric pulses was visualized with a Zeiss LSM 710 inverted confocal microscope, using a 100x oil immersion objective (Ph2, Archoplan, 100x/1.25 Oil) to image both the lipid bilayer and the actin cortex. Two different pulsing protocols were used: (i) consecutive increasing pulses starting from low fields, increasing gradually to higher fields (ranging from $10 - 300$ V/mm with steps of approximately 10 V/mm), (ii) immediate high pulses (ranging from $300 - 1000$ V/mm with steps of approximately 200 V/mm), where only 2 to 4 pulses were applied of increasing field. In both cases 500 μs pulses were used, with approximately 1 minute interval between the pulses. The first pulse protocol (i) was used to test the onset of the breakdown of the actin cortex. The second pulse protocol (ii) was used to decouple the breakdown of the actin cortex from the cumulative effect of the multiple consecutive pulses. A z-stack of 7 focal planes, with a range of approximately the diameter of the GUV (Δz $\sim$ 4 μm), of the fluorescence signal of the membrane and the actin was taken before and after the pulses, to record the response of the actin cortex. The z-stack imaging is a slow technique (approximately 5 to 10 seconds time interval in between the z-stacks), so only the GUV size and the actin cortex stability before and after the pulse can be extracted.

2.5 Data analysis of GUVs response

The bright field images of the GUVs were analyzed by a custom written Matlab script. The contours of the GUVs were detected with the Canny edge detection method and fitted to an ellipse to extract the equatorial (a) and polar (b, the distance from the center to the poles of

a spheroid) radii of the GUVs. For the dynamics studies, these two radii were used to obtain the deformation ratio (a/b) during and after the pulse. Afterwards, the time-dependent deformation was fitted to an exponential decay curve to obtain the relaxation time(s) of the GUVs, similar to the method reported by Riske and Dimova (41) (Figure 2).

During the confocal experiments, multiple planes of the GUVs were imaged. The radius of the GUVs was determined from the fluorescent confocal membrane images taken at the equatorial plane of the GUV by a similar detection method as described above. These images were used to reveal the area loss of the GUVs as a function of electric field. In order to remove spurious effects due to motion of the GUV in and out of the imaging plane, the normalized area ($\mathrm{A_{norm}}$) was calculated at pulse n and corrected for the area loss at the previous pulse $(n-1)$: $\mathrm{A_{norm}} = (\mathrm{A_f}/\mathrm{A_i})_\mathrm{n}(\mathrm{A_f}/\mathrm{A_i})_{\mathrm{n}-1}$. Here, $\mathrm{A_i}$ and $\mathrm{A_f}$ represent the initial and the final area of the GUV before (initial) and after (final) the pulse, respectively. $(\mathrm{A_f}/\mathrm{A_i})_\mathrm{n}$ and $(\mathrm{A_f}/\mathrm{A_i})_{\mathrm{n}-1}$ are the normalized areas of the GUV at the pulse n and at the preceding pulse $(n-1)$. By multiplying these two factors, the normalized area is corrected for shrinkage due to earlier pulses. Additionally, the intensity of the fluorescence signal of the actin was obtained from confocal z-stacks by determining the mean and average intensity of all planes. Photobleaching of the actin cortex was removed by correcting the data at scan number k with a reference of a separate photobleaching experiment of a GUV without applying any pulses. By normalizing the actin fluorescence intensity from the bleaching experiment, the correction factor for the photobleaching per scan is calculated ($\mathrm{I_{ref,k}} = \mathrm{I_{k,ref}}/\mathrm{I_{0,ref}}$, where $\mathrm{I_{0,ref}}$ and $\mathrm{I_{k,ref}}$ are the intensities of the image at the start of the photobleaching experiment and at the relevant scan number k, respectively). Consequently, the results of the electroporation experiments were corrected as follows: $\mathrm{I_{norm}} = \mathrm{I_k}/(\mathrm{I_0}\mathrm{I_{ref,k}})$. Again, $\mathrm{I_0}$ and $\mathrm{I_k}$ represent the intensities of the image at the start of the experiment and at scan number k, respectively, in this case during an electroporation experiment (see Figure S.1 in the supplementary material).

3 Results and discussion

3.1 The dynamics of the GUVs

To investigate the influence of the actin cortex on the electroporation of GUVs, we captured the dynamics of the GUVs by high speed imaging ($10\,000 - 15\,000$ fps) in bright field. The deformations of the GUVs were measured in the terms of the deformation ratio a/b during and after the electric pulse (see the schematic in Figure 2). The GUVs are electroporated above a certain threshold field, as the accumulated transmembrane voltage exceeds a threshold voltage. GUVs exposed to electroporative pulses, above the critical field, could be recognized by the observation of a macropore or the contrast loss due to the exchange of glucose and sucrose molecules between the interior and exterior of the GUV. Below the critical threshold field, where no macropores nor contrast loss have been observed, the GUVs exhibited squarelike deformations, as shown in Figure 2A. These deformations relax back exponentially with a characteristic relaxation time (τ_1) in the order of 100 μs for both the

empty and the actin-encapsulated GUVs. Riske and Dimova (55) have shown that the presence of the ions flattens the membrane, which they attributed mainly to the electrophoretic forces of the ions, leading to squarelike deformations. The conductivity ratio χ is defined as the ratio between the conductivity of the internal (λ_{in}) and external solution of the vesicle (λ_{out}), $\chi = \lambda_{\text{in}}/\lambda_{\text{out}}$. Depending on this conductivity ratio, vesicles are expected to either deform along the field, referred to as a tubelike shape, (a/b > 1, $\chi > 1$) or perpendicular to the field, referred to as a disklike shape, (a/b < 1, $\chi < 1$). We observed both disklike and tubelike deformations during the pulsing experiments of both the empty and the actin-encapsulated GUVs. It must be noted that an ionophore is used to transport Mg^{2+} into the GUVs to initiate actin polymerization and cortex formation after the GUV formation, as discussed in the methods section. Some variation in the conductivity of the inner solution of the GUVs is possible due to our preparation method, which would explain the observations of both disklike and tubelike deformations. Additionally, permeabilizing pulses cause an exchange of the inner and outer solutions, and consequently may alter the conductivities of the two solutions. As these observations are similar for both the empty and actin-encapsulated GUVs, they can be related to the presence of the ionophore and the ion-imbalance of the inner and outer solution.

The response of the empty and the actin-encapsulated GUVs to an electroporative pulse was strikingly different, as shown in Figure 2. Macropores were observed for the empty GUVs, as was reported before (41). Additionally, we observed a characteristic relaxation process, where the relaxation of the macropore (with a duration τ_2 of $\sim$ 1 ms) was followed by a subsequent relaxation (with a duration duration τ_3 of $\sim$ 10 ms), as illustrated in Figure 2B and movie S1. The observation of the latter relaxation time τ_3 (see Figure 2B3) did not always occur during macropore formation. This response is similar to earlier reports for empty GUVs composed of egg phosphatidylcholine by Riske and Dimova (41). They attributed τ_2 to the relaxation time of the macropore in a non supported lipid bilayer($\tau_{\text{pore}} \sim \eta_{\text{s}}\text{r}/(2\gamma)$, where η_{s} is the surface viscosity) and τ_3 to the relaxation of the membrane due to either the excess surface area of the GUVs or an increase of the excess area during the macroporation (41).

The distributions of the different relaxation times in the non-porative and porative regimes are shown in Figure 3A for both the empty and actin-encapsulated GUVs. In strong contrast to the observations of the macropores and large deformations for the empty GUVs, the actin-encapsulated GUVs show only small deformations during the electroporative pulses and do not exhibit macropores (Figure 2C and movie S2). Moreover, the relaxation time τ_2 of the actin-containing GUVs is in the same order as that of the empty GUVs ($\sim$ 800 μs), as shown in Figure 3A. Since no macroporation was observed for these GUVs, electropermeabilization was determined by the contrast loss of the GUVs. This contrast loss indicates the permeabilization of the membrane, due to the exchange of molecules through the membrane. All empty GUVs required multiple pulses ($\sim$ 7 pulses) in order to loose complete contrast, indicating a relatively short permeabilization state where only little exchange of molecules is possible. On the contrary, almost all actin-encapsulated GUVs (13 out of 15 GUVs) exhibited complete contrast loss within a few minutes after the first pulse, demonstrating a longer lasting permeabilization of the actin-supported membrane. Due to limited recording time

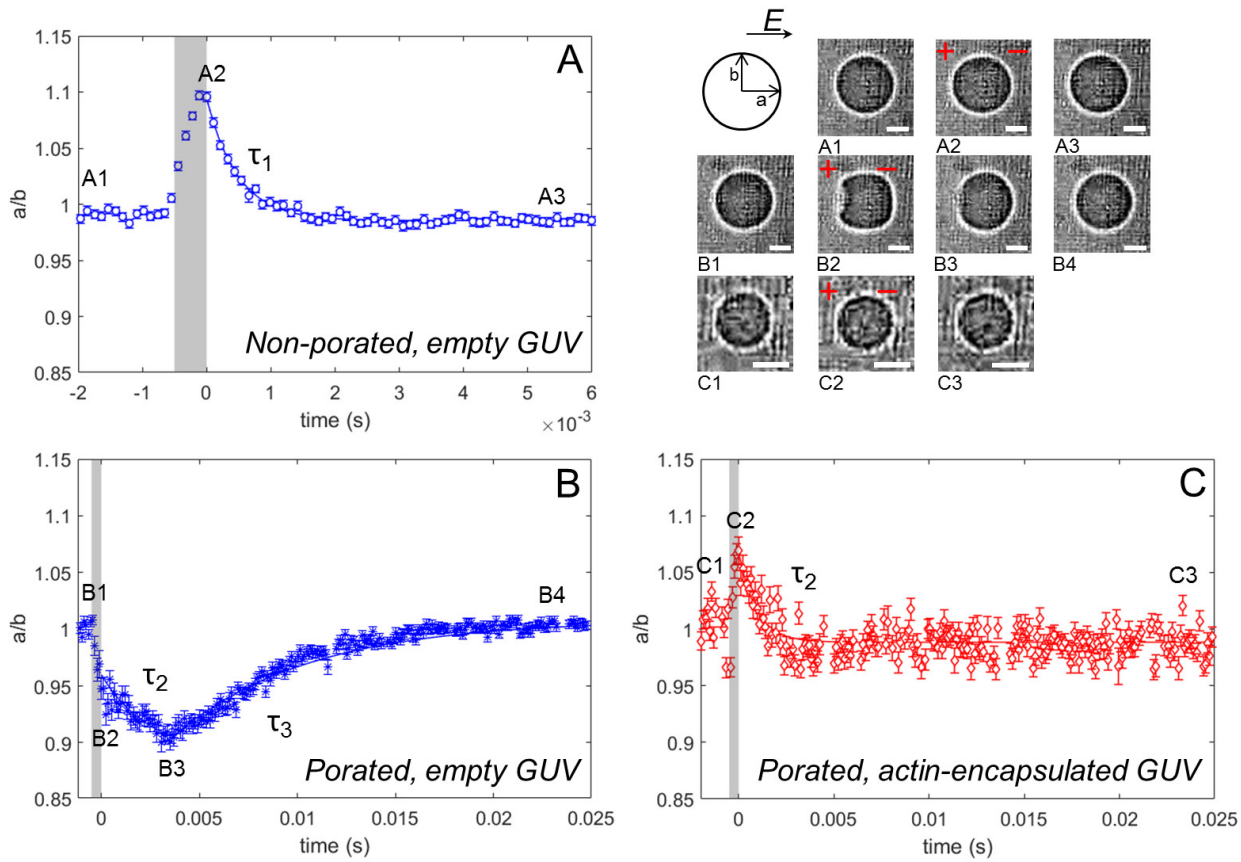

Figure 2: The dynamics of GUVs with and without an encapsulated actin cortex. (A) The dynamics of a non-porated empty GUV, where deformation and a single relaxation (τ_1) is observed. (B) The dynamics of a porated empty GUV, where a pore is observed together with a double relaxation (τ_2 and τ_3). (C) The dynamics of a porated actin-encapsulated GUV where no macropore is observed, and only a single relaxation (τ_2).The relaxation times are obtained from exponential fits to the deformation data, as explained in the text. The scale bar in all images is 5 μm. The definitions of non-porated and porated GUVs are explained in the text.

of the high-speed imaging in the experiments (maximum of 2 seconds), no dynamics of the contrast loss was captured. The relaxation time τ_2, which shows the time-dependent deformation of the actin-encapsulated GUVs in the electroporative regime, is comparable to the relaxation time τ_2 of the empty GUVs (Figure 3 A). However, the slow dynamics of the contrast loss after a pulse for the actin-containing GUVs indicates that the membrane remains permeabilized up to minutes, which was not observed for the empty GUVs. Moreover, no macropores have been observed. Therefore, the pore resealing time of the actin-encapsulated GUVs cannot be deduced from τ_2, due to the absence of macropores and the slow resealing process which occurs in the presence of the actin cortex. This slow resealing process is consistent with observations in cells (21, 22). However, in cells it appeared that the role of the actin cortex is limited to the resealing of the permeated structures, and does not involve the nucleation and expansion process. On the contrary, we observed in GUVs that an actin cortex prevents the formation of macropores, indicating that the expansion of the pores is restricted. Similarly, studies on living cells have proposed that the formed electropores in the membrane cannot expand beyond the mesh size of the actin network (18, 50). In conclusion, the presence of the actin cortex in the GUVs limits the growth of the pores to microscopically unobservable sizes ($< 1\,\mu$m), and slows down their resealing.

As discussed above, we observed both disklike (a/b < 1) and tubelike (a/b > 1) deformations for the empty and the actin-encapsulated GUVs. The broad distribution of the maximum deformation $(a/b)_{max}$ at the end of the pulse is shown in Figure 3B. For both types of GUVs, the majority of the GUVs undergoes tubelike deformation, indicating a higher conductivity of the interior of the GUVs and thus a proper transport of the Mg^{2+} ions across the membrane by the ionophore. The deformations of the actin-encapsulated GUVs are significantly smaller than those of the empty GUVs, which can be seen from the more narrow distribution of $(a/b)_{max}$ (shown in red in Figure 3B). The wide distribution observed for $(a/b)_{max}$ of the GUVs is caused by the preparation technique used for making the actin-encapsulated GUVs. It offers a poor control on the membrane tension of the GUVs (both for the empty and the actin-encapsulated GUVs). Moreover, the actin-encapsulated GUVs likely possess different actin cortex thicknesses, leading to different mechanical properties (54). On average, the actin-encapsulated GUVs express less pronounced deformations than the empty GUVs, as shown in Figure 3B. Experiments on GUVs in alternating current (AC) fields have shown that the deformation of the GUVs can be related to the bending rigidity of the membrane (57). Additionally, in DC field experiments, non-electroporative pulses can be used to study the stiffness of the membrane, where the relaxation of the GUVs gives insight in the mechanical properties of the membrane (58). In our experiments we focused on pulses around the transmembrane voltage of 1V, therefore we cannot derive the precise mechanical properties. Nevertheless, the smaller deformations of the GUVs with an encapsulated actin cortex clearly signify an increase in the bending rigidity of the GUVs, consistent with previous research works showing that the actin cortex leads to an increased bending rigidity (54, 59, 60). In conclusion, our results show that the presence of an actin cortex prevents macropore formation and reduces membrane deformation, which may contribute to the differences observed between the response of cells and empty GUVs to electric

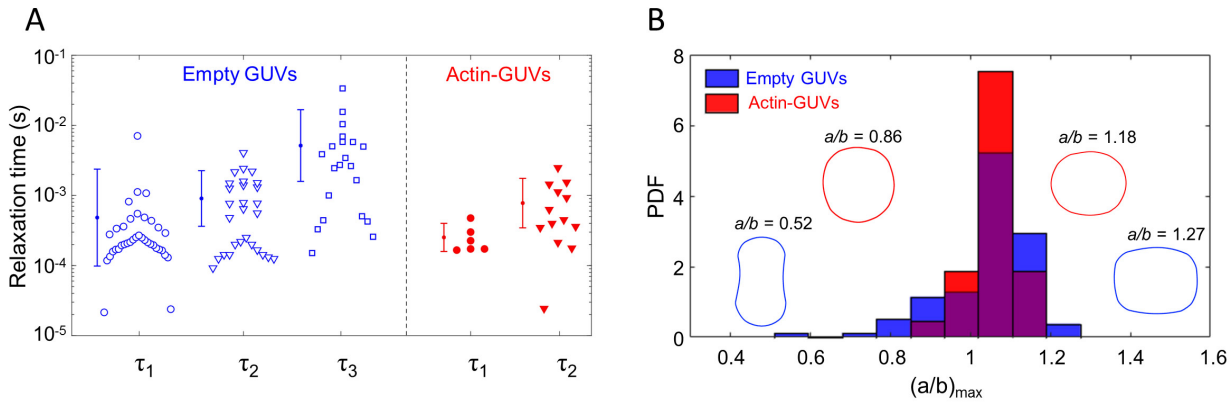

Figure 3: (A) Relaxation times of empty (blue open symbols) and actin-encapsulated (red filled symbols) GUVs in the non-electroporative regime (τ_1) and the electroporative regime (τ_2 and τ_3). (B) The distribution of the maximum deformations of empty (blue) and actin-encapsulated (red) GUVs during all pulses (both electroporative and non-electroporative). The schematics in the histogram represent simplified contours of the corresponding disklike and tubelike deformations, not to scale. The data in both panels is of 16 actin-encapsulated GUVs with an average radius of ~ 5 μm and 10 empty GUVs with an average radius of ~ 5 μm.

pulses.

3.2 Stability of the actin cortex

To assess the response of the actin cortex inside the GUV to the electric pulse, the GUV and actin were concurrently visualized by confocal microscopy. The fluorescence signals of the membrane and actin cortex were used to detect the area of the GUV and the actin cortex intensity, respectively (see Figure S.2 in the supplementary material). In order to determine the coverage of the actin cortex on the inner membrane surface and any possible angular dependent response of the actin (i.e. lateral inhomogeneities of the cortex due to the distribution of the induced transmembrane voltage on the membrane of the GUV), a confocal z-stack was taken before and after the pulse. Consecutive pulses of increasing voltage were applied to the GUVs, with at least 1 minute in between the pulses to minimize the effect of the former pulse. Similar to earlier studies (12, 40, 44, 61), the empty GUVs exhibit increasing shrinkage with higher electric pulses (Figure 4A). The immediate high pulses reveal the cumulative effect of multiple pulses on the shrinkage of the empty GUVs. A single pulse of 300 V/mm does not induce the same shrinkage as a 300 V/mm pulse preceded by multiple pulses at lower field strength (see Figure 4A). Recent work has shown that the shrinkage of the GUVs is dependent on the surface viscosity of the bilayer (49). Compared to the empty GUVs, the actin-encapsulated GUVs display shrinkage at higher electric fields, i.e. the actin-supported bilayer has a higher electrical stability (Figure 4B).

Strikingly, the increasing pulses also result in a decreasing fluorescence signal of the actin

at $\sim$ 150 V/mm, followed by GUV shrinkage at higher electric pulses ($\sim$ 200 V/mm). An example GUV is shown in Figure 4B and Movie S3 to provide microscopic insight in the response of the actin fluorescence signal. As shown, the decrease in the fluorescence signal of the actin can be associated with a breakdown of the actin cortex. Additionally, the intensity loss of the actin cortex due to the electric pulses appears to be slightly more at the poles where the GUV is facing the electrodes (Movie S3). However, this radial dependence is not always observed clearly, perhaps because the GUVs can rotate due to the pulse. After the breakdown of the actin cortex we did not observed any increase in the bulk intensity of the GUV (see Section S.3 and Figure S.2 in the supplementary material). By recording the photobleaching of the actin signal in the absence of the pulse and also the response of GUVs with encapsulated actin cortex to immediate high pulses, we could confirm that the fluorescence decrease is caused by the breakdown of the cortex and is not a side effect of bleaching. This notion is further supported by the observation that after the pulse the actin fluorescence signal progressively decreases for several tens of seconds. This gradual decrease in the signal indicates a slow breakdown of the actin cortex. In addition, the shrinkage of the actin-encapsulated GUVs at higher electric fields than of the empty GUVs indicates that initially the actin cortex stabilizes the membrane and that shrinkage can take place after the breakdown of the cortex.

Similar results have been observed for human cell lines (23) and plant cells (24) exposed to nanosecond pulsed electric fields (nsPEF). The nanosecond pulses affect the actin cytoskeleton, which is attributed to depolymerization of the filaments (23, 24). For plant cells it was reported that nanosecond pulses induce disassembly of the actin (24, 62). On the contrary, Pakhomov et al. (30) have shown for CHO cells that the depolymerization of the actin cortex is due to osmotic swelling of the cells upon electropermeabilization. However, Tolstykh et al. (63) have proposed that additional biological processes are involved in actin depolymerization, involving the depletion of phosphatidylinositol-4,5-biphosphate (PIP_2) lipids. By studying GUVs with an encapsulated actin cortex, we have eliminated the biological processes from our results. Additionally, no osmotic swelling is observed in our experiments. On the other hand, the small deformations of the actin-encapsulated GUVs observed in bright field dynamics studies (Figure 4B) can lead to an induced membrane tension. Therefore, we need to consider both the mechanical forces, originating from the induced electrical membrane stress during the pulse, and the electrophoretic forces acting on the actin filaments as soon as the membrane is permeabilized to explain the depolymerization of the actin cortex in the GUVs.

In order to find the origin of the actin cortex depolymerization, we estimate the magnitude of possible forces acting on the actin filaments. When immersed in a solution, actin monomers polymerize into semi-flexible filaments of different lengths that collectively form an entangled network. The total number of filaments underneath the lipid bilayer can be estimated (64) as:

$$\mathrm{N_f} \sim \frac{\mathrm{c_0} \times \frac{4}{3}\pi \mathrm{R}^3 \times \mathrm{d}}{\mathrm{l}} \tag{3}$$

where c_0 and d are the initial concentration ($4.2 \times 10^{21}\,\mathrm{m}^{-3}$) and size of actin monomers,

l is the average length of filaments. Assuming the filaments have a length in the order of the actin shell thickness (i.e., $l \sim 1 - 4\mu$m, see Figure S.3 in the supplementary material) and with $R = 5 - 10\ \mu$m and $d = 2.5$ nm, we estimate the total number of filaments to be $N_f \sim 10^4$. The mesh size of the filament network can be approximated as: $\zeta \sim \sqrt{\frac{A}{N_f}}$ with A being the surface area of the membrane. The amount of stretch imposed on the length of connections in the actin network reads:

$$\Delta\zeta = \zeta_{\text{Ellipsoid}} - \zeta_{\text{Sphere}}. \tag{4}$$

As the total enclosed volume of the GUVs is conserved during their deformation into ellipsoidal topologies in the experiments, the equatorial and polar radii become $b = e^{-1/3}R$ and $a = e^{2/3}R$, respectively, where $e = \sqrt{a/b}$ is taken from the example GUV shown in the schematic in Figure 3B. We choose a value of $e \sim 1.18$, corresponding to the maximum deformation experienced by the GUVs. The total surface area of the GUVs increases during the deformation and hence the concomitant mesh size stretches by $\Delta\zeta \sim 0.0005 - 0.001$ nm (if we assume affine deformations for the network). Such an increase in the length of interconnected filaments induces a mechanical force of the order of $f_m \sim 17 - 48$ pN for a stretching stiffness of ~ 43 pN/nm (65, 66). This value is markedly smaller than the previously reported force values needed for either initiating the depolymerization of a filament network (67) or the rupture of single filaments (68), which are in the range of $\sim 100 - 400$ pN. It is, therefore, unlikely that the mechanical forces generated by in-plane tensions are the only origin of the breakdown of the actin cortex in our experiments. Other mechanisms, including electrophoretic forces, are expected to be involved.

As soon as the membrane is permeabilized by the electric fields, the membrane tension can relax back through the expansion of the pores and the release of the interior fluid. Additionally, the actin cortex is exposed to the electric field and consequently actin filaments experience an electrophoretic force, defined as (69):

$$f_{\text{electrophoretic}} = \xi_h \mu_B E \tag{5}$$

where ξ_h and μ_B represent the hydrodynamic friction coefficient per unit length of a filament close to the surface and the electrophoretic mobility of the actin measured in bulk solution, respectively. By assuming an average length of the actin filaments of $1 - 4\ \mu$m and an interaction of the complete filament with the membrane, due to Mg^{2+}-mediated adhesion, the force per unit length can be converted in the electrophoretic force $f_{\text{electrophoretic}}$. The maximum force experienced by the actin filaments corresponds to a condition in which the filaments are perpendicular to the field. As soon as the GUV is permeabilized and micro/macropores are formed, the electric field penetrates into the GUV, with a maximum value of $\sim 0.8E$ and $\sim 0.1E$ at the regions perpendicular and parallel to the field, respectively (see Figure S.5 in the supplementary material). The fluorescence signal of the actin cortex drops at approximately 150 V/mm (Figure 4A). At this electric field and considering a hydrodynamic friction of $\zeta = 0.034$ N.s/m^2 (for cytoplasmic fluid motion perpendicular to the filament length (70)) and an electrophoretic mobility of $\mu_B = 10^{-8}$ m^2/(V.s), we predict an electrophoretic force of $f_{\text{electrophoretic}} \sim 80 - 160$ pN acting on a single filament.

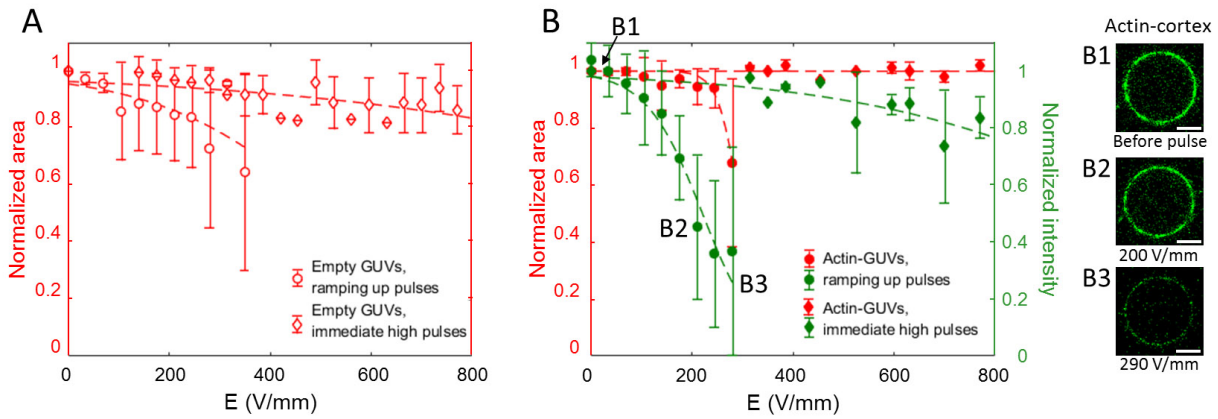

Figure 4: The structural stability of the empty and the actin-encapsulated GUVs. (A) The area loss of the empty GUVs as a function of electric field. The average normalized area is shown of 15 empty GUVs in total with an average radius of ~ 10 μm, of which 9 have been exposed to the consecutive ramping up pulses and 5 to immediate high pulses. (B) The area loss of the actin-encapsulated GUVs as a function of the electric field, which is associated with an intensity loss of the actin cortex. The average normalized area is shown of 17 actin-encapsulated GUVs in total with an average radius of ~ 10 μm, of which 8 have been exposed to the consecutive ramping up pulses and 9 to immediate high pulses. The confocal images of the actin cortex show that the intensity loss can be attributed to cortex disruption (B1, B2 and B3). The dotted lines in the graphs represent a least-squares fit of a sigmoid curve to guide the eye. The scale bar in all images is 5 μm.

Compared to the mechanical forces calculated above, these forces appear most plausible to initiate depolymerization of the actin cortex. Moreover, the depolymerization of the cortex mostly occurs above the critical transmembrane voltage (see Figure S.6 in the supplementary material), enabling the electrophoretic forces to affect the actin filaments.

4 Conclusion

To reveal the role of the actin cortex during electroporation of cells, we have prepared GUVs with an encapsulated actin cortex and exposed them to electric pulses. Both the response of the actin cortex and the dynamics of the GUV during and after the pulse have been imaged. Our results show that the actin cortex inhibits large deformation of the GUVs during the electric pulses. This inhibition could be due to rigidification of the membrane by the presence of the actin cortex (54). Additionally, the actin cortex prevents the formation of large pores, referred to as macropores, due to the restricted mobility of the lipids attached to the actin network. At higher electric fields, the cortex is depolymerized due to the electric pulses. Based on the estimation of the relevant forces, we suggest that the depolymerization (or disruption) is predominantly triggered by the electrophoretic forces on the actin filaments

during the pulses.

Our results also indicate that current simplified models of cell-like environments (such as empty GUVs) need to be extended with an actin network in order to more closely mimic the plasma membrane and elucidate the role of the actin cortex in electroporation. This modification is also essential for a better understanding of the different stages of the electroporation process. For example, there are known to be major differences in pore size, the occurrence of lipid loss and pore dynamics between living cells and GUVs during electroporation. Therefore, the actin-supported GUVs enable exploring the behavior of more complex systems, such as the dynamics of the electropores and the mechanism of electro-gene transfection.

Supporting citations

References (71–75) appear in the Supplementary Material.

Acknowledgments

DLP, AV, LR, and PEB thank the European Research Council (ERC) under the European Unions Seventh Framework Programme (FP/2007-2013), grant agreement No 337820 (E-DNA-T-PEP). YM and GHK were supported by the European Research Council (ERC) from an ERC Starting Grant (335672-MINICELL). The authors thank Shaurya Sachdev and Aswin Muralidharan for critical reading of the manuscript.

References

[1] Haase, K., and A. E. Pelling. 2013. The role of the actin cortex in maintaining cell shape. *Communicative & integrative biology*. 6:e26714.

[2] Salbreux, G., G. Charras, and E. Paluch. 2012. Actin cortex mechanics and cellular morphogenesis. *Trends in cell biology*. 22:536–45.

[3] Simon, C., R. Kusters, V. Caorsi, A. Allard, M. Abou-Ghali, J. Manzi, A. Di Cicco, D. Levy, M. Lenz, J.-F. Joanny, et al. 2018. A direct proof that sole actin dynamics drive membrane deformations. *bioRxiv*. :307173.

[4] Heinemann, F., S. K. Vogel, and P. Schwille. 2013. Lateral membrane diffusion modulated by a minimal actin cortex. *Biophysical journal*. 104:1465–1475.

[5] Honigmann, A., S. Sadeghi, K. Jan, S. W. Hell, C. Eggeling, and R. Vink. 2014. A Lipid Bound Actin Meshwork Organizes Liquid Phase Separation in Model Membranes. *Biophysical Journal*. 106:634a.

[6] Bray, D., and J. White. 1988. Cortical flow in animal cells. *Science*. 239:883–888.

[7] Towhidi, L., T. Kotnik, G. Pucihar, S. M. P. Firoozabadi, H. Mozdarani, and D. Miklavčič. 2008. Variability of the minimal transmembrane voltage resulting in detectable membrane electroporation. *Electromagnetic Biology and Medicine*. 27:372–385.

[8] Teissie, J., M. Golzio, and M. Rols. 2005. Mechanisms of cell membrane electropermeabilization: a minireview of our present (lack of ?) knowledge. *Biochimica et Biophysica Acta (BBA) - General Subjects*. 1724:270–280.

[9] Rols, M., and J. Teissié. 1990. Electropermeabilization of mammalian cells. Quantitative analysis of the phenomenon. *Biophysical Journal*. 58:1089–1098.

[10] Lopez, A., M. Rols, and J. Teissie. 1988. ^{31}P NMR Analysis of Membrane Phospholipid Organization In Viable, Reversibly Electropermeabilized Chinese Hamster Ovary Cells. *Biochemistry*. 27:1222–1228.

[11] Kinosita, J., Kazuhiko, and Y. Tsong, Tian. 1977. Voltage-induced pore formation and hemolysis of human erythrocytes. *Biochimica et Biophysica Acta (BBA) - Biomembranes*. 471:227–242.

[12] Tekle, E., R. D. Astumian, W. A. Friauf, P. B. Chock, R. Huber, K. Nagayama, K. Ikegami, R. Gilbert, L. Mir, and D. Reintgen. 2001. Asymmetric pore distribution and loss of membrane lipid in electroporated DOPC vesicles. *Biophysical journal*. 81:960–968.

[13] Benz, R., and U. Zimmermann. 1980. 376 - Relaxation studies on cell membranes and lipid bilayers in the high electric field range. *Bioelectrochemistry and Bioenergetics*. 7:723–739.

[14] Teissie, J., and T. Tsong. 1981. Electric Field Induced Transient Pores in Phospholipid Bilayer Vesicles. *Biochemistry*. 20:1548–1554.

[15] Sowers, A. 1987. The long-lived fusogenic state induced in erythrocyte ghosts by electric pulses is not laterally mobile. *Biophysical Journal*. 52:1015–1020.

[16] Weaver, J. C. 1995. Electroporation Theory. *In* Animal Cell Electroporation and Electrofusion Protocols. J. A. Nickoloff, editor. Humana Press, Totowa, NJ, pp. 3–28.

[17] Perrier, D. L., L. Rems, and P. E. Boukany. 2017. Lipid vesicles in pulsed electric fields: fundamental principles of the membrane response and its biomedical applications. *Advances in Colloid and Interface Science*. 249:248–271.

[18] Weaver, J. C., and Y. Chizmadzhev. 1996. Theory of electroporation: A review. *Bioelectrochemistry and Bioenergetics*. 41:135–160.

[19] Rosazza, C., A. Buntz, T. Rieß, D. Wöll, A. Zumbusch, and M.-P. Rols. 2013. Intracellular Tracking of Single-plasmid DNA Particles After Delivery by Electroporation. *Molecular Therapy*. 21:2217–2226.

[20] Rosazza, C., S. H. Meglic, A. Zumbusch, M.-P. Rols, and D. Miklavcic. 2016. Gene Electrotransfer: A Mechanistic Perspective. *Current Gene Therapy*. 16:98–129.

[21] Rols, M.-P., and J. Teissié. 1992. Experimental evidence for the involvement of the cytoskeleton in mammalian cell electropermeabilization. *Biochimica et Biophysica Acta (BBA) - Biomembranes*. 1111:45–50.

[22] Teissié, J., and M.-P. Rols. 1994. Manipulation of Cell Cytoskeleton Affects the Lifetime of Cell Membrane Electropermeabilization. *Annals of the New York Academy of Sciences*. 720:98–110.

[23] Stacey, M., P. Fox, S. Buescher, and J. Kolb. 2011. Nanosecond pulsed electric field induced cytoskeleton, nuclear membrane and telomere damage adversely impact cell survival. *Bioelectrochemistry*. 82:131–134.

[24] Berghöfer, T., C. Eing, B. Flickinger, P. Hohenberger, L. H. Wegner, W. Frey, and P. Nick. 2009. Nanosecond electric pulses trigger actin responses in plant cells. *Biochemical and Biophysical Research Communications*. 387:590–595.

[25] Hohenberger, P., C. Eing, R. Straessner, S. Durst, W. Frey, and P. Nick. 2011. Plant actin controls membrane permeability. *Biochimica et Biophysica Acta (BBA) - Biomembranes*. 1808:2304–2312.

[26] Thompson, G. L., C. Roth, G. Tolstykh, M. Kuipers, and B. L. Ibey. 2014. Disruption of the actin cortex contributes to susceptibility of mammalian cells to nanosecond pulsed electric fields. *Bioelectromagnetics*. 35:262–272.

[27] Xiao, D., L. Tang, C. Zeng, J. Wang, X. Luo, C. Yao, and C. Sun. 2011. Effect of actin cytoskeleton disruption on electric pulse-induced apoptosis and electroporation in tumour cells. *Cell Biology International*. 35:99–104.

[28] Stacey, M., J. Stickley, P. Fox, V. Statler, K. Schoenbach, S. J. Beebe, and S. Buescher. 2003. Differential effects in cells exposed to ultra-short, high intensity electric fields: cell survival, DNA damage, and cell cycle analysis. *Mutation research*. 542:65–75.

[29] Mahlke, M. A., C. Navara, and B. L. Ibey. 2014. Effects of nanosecond pulsed electrical fields (nsPEFs) on the cell cycle of CHO and Jurkat cells. volume 8941. International Society for Optics and Photonics. 89411R.

[30] Pakhomov, A. G., S. Xiao, O. N. Pakhomova, I. Semenov, M. A. Kuipers, and B. L. Ibey. 2014. Disassembly of actin structures by nanosecond pulsed electric field is a downstream effect of cell swelling. *Bioelectrochemistry*. 100:88–95.

[31] Chopinet, L., and M.-P. Rols. 2015. Nanosecond electric pulses: A mini-review of the present state of the art. *Bioelectrochemistry*. 103:2–6.

[32] Abidor, I., V. Arakelyan, L. Chernomordik, Y. Chizmadzhev, V. Pastushenko, and M. Tarasevich. 1979. Electric breakdown of bilayer lipid membranes: I. The main experimental facts and their qualitative discussion. *Journal of Electroanalytical Chemistry and Interfacial Electrochemistry*. 104:37–52.

[33] van Uitert, I., S. Le Gac, and A. van den Berg. 2010. Determination of the electroporation onset of bilayer lipid membranes as a novel approach to establish ternary phase diagrams: example of the l-α-PC/SM/cholesterol system. *Soft Matter*. 6:4420–4429.

[34] Sengel, J. T., and M. I. Wallace. 2016. Imaging the dynamics of individual electropores. *Proceedings of the National Academy of Sciences of the United States of America*. 113:5281–5286.

[35] Dimova, R., K. A. Riske, S. Aranda, N. Bezlyepkina, R. L. Knorr, and R. Lipowsky. 2007. Giant vesicles in electric fields. *Soft Matter*. 3:817–827.

[36] Dimova, R., N. Bezlyepkina, M. D. Jordo, R. L. Knorr, K. A. Riske, M. Staykova, P. M. Vlahovska, T. Yamamoto, P. Yang, and R. Lipowsky. 2009. Vesicles in electric fields: some novel aspects of membrane behavior. *Soft Matter*. 5:3201–3212.

[37] Portet, T., C. Mauroy, V. Démery, T. Houles, J.-M. Escoffre, D. S. Dean, and M.-P. Rols. 2012. Destabilizing giant vesicles with electric fields: an overview of current applications. *The Journal of Membrane Biology*. 245:555–564.

[38] Powell, K. T., and J. C. Weaver. 1986. Transient aqueous pores in bilayer membranes: A statistical theory. *Bioelectrochemistry and Bioenergetics*. 15:211–227.

[39] Needham, D., and R. M. Hochmuth. 1989. Electro-mechanical permeabilization of lipid vesicles. Role of membrane tension and compressibility. *Biophysical Journal*. 55:1001–1009.

[40] Portet, T., R. Dimova, M. Zuckermann, and e. al. 2010. A new method for measuring edge tensions and stability of lipid bilayers: effect of membrane composition. *Biophysical journal*. 99:3264–3273.

[41] Riske, K. A., and R. Dimova. 2005. Electro-deformation and poration of giant vesicles viewed with high temporal resolution. *Biophysical Journal*. 88:1143–1155.

[42] Isambert, H. 1998. Understanding the Electroporation of Cells and Artificial Bilayer Membranes. *Physical Review Letters*. 80:3404–3407.

[43] Smith, K., C., J. Neu, C., and W. Krassowska. 2004. Model of Creation and Evolution of Stable Electropores for DNA Delivery. *Biophysical Journal*. 86:2813–2826.

[44] Portet, T., F. Camps i Febrer, J.-M. Escoffre, C. Favard, M.-P. Rols, and D. S. Dean. 2009. Visualization of membrane loss during the shrinkage of giant vesicles under electropulsation. *Biophysical Journal*. 96:4109–4121.

[45] Sadik, M. M., J. Li, J. W. Shan, D. I. Shreiber, and H. Lin. 2011. Vesicle deformation and poration under strong dc electric fields. *Physical Review E*. 83:66316.

[46] Kinosita, K., M. Hibino, H. Itoh, M. Shigemori, K. Hirano, Y. Kirino, and T. Hayakawa. 1992. 3 Events of membrane electroporation visualized on a time scale from microsecond to seconds. *In* Guide to electroporation and electrofusion. B. M. Chassy, J. A. Saunders, and A. E. Sowers, editors. Academic Press, Inc., pp. 29–46.

[47] Moroz, D., J., and P. Nelson. 1997. Dynamically stabilized pores in bilayer membranes. *Biophysical Journal*. 72:2211–2216.

[48] Knorr, R. L., M. Staykova, R. S. Gracia, and R. Dimova. 2010. Wrinkling and electroporation of giant vesicles in the gel phase. *Soft Matter*. 6:1990–1996.

[49] Perrier, D. L., L. Rems, M. T. Kreutzer, and P. E. Boukany. 2018. The role of gel-phase domains in electroporation of vesicles. *Scientific Reports*. 8:4758.

[50] Chang, C., Donald, and S. Reese, Thomas. 1990. Changes in membrane structure induced by electroporation as revealed by rapid-freezing electron microscopy. *Biophysical Journal*. 58:1–12.

[51] Dimitrov, S., Dimiter, and E. Sowers, Arthur. 1990. Membrane electroporaton fast molecular exchange by electroosmosis. *Biochimica et Biophysica Acta (BBA) - Biomembranes*. 1022:381–392.

[52] Weaver, C., James, I. Harrison, Gail, G. Bliss, Jonathan, R. Mourant, Judith, and T. Powell, Kevin. 1988. Electroporation: High frequency of occurrence of a transient high-permeability state in erythrocytes and intact yeast. *FEBS Letters*. 229:30–34.

[53] Tekle, E., R. D. Astumian, and P. B. Chock. 1994. Selective and asymmetric molecular transport across electroporated cell membranes. *Proceedings of the National Academy of Sciences*. 91:11512–11516.

[54] Schäfer, E., M. Vache, T.-T. Kliesch, and A. Janshoff. 2015. Mechanical response of adherent giant liposomes to indentation with a conical AFM-tip. *Soft Matter*. 11:4487–4495.

[55] Riske, K. A., and R. Dimova. 2006. Electric Pulses Induce Cylindrical Deformations on Giant Vesicles in Salt Solutions. *Biophysical Journal*. 91:1778–1786.

[56] Kotnik, T., and G. Pucihar. 2010. Chapter 3. Induced transmembrane voltage-theory, modeling, and experiments. *In* Advanced electroporation techniques in biology and medicine. A. G. Pakhomov, D. Miklavčič, and M. S. Markov, editors. CRC Press, pp. 51–70.

[57] Gracia, R. S., N. Bezlyepkina, R. L. Knorr, R. Lipowsky, and R. Dimova. 2010. Effect of cholesterol on the rigidity of saturated and unsaturated membranes: fluctuation and electrodeformation analysis of giant vesicles. *Soft Matter*. 6:1472–1482.

[58] Yu, M., R. B. Lira, K. A. Riske, R. Dimova, and H. Lin. 2015. Ellipsoidal Relaxation of Deformed Vesicles. *Physical Review Letters*. 115:128303.

[59] Guevorkian, K., J. Manzi, L.-L. Pontani, F. Brochard-Wyart, and C. Sykes. 2015. Mechanics of Biomimetic Liposomes Encapsulating an Actin Shell. *Biophysical Journal*. 109:2471–2479.

[60] Häckl, W., M. Bärmann, and E. Sackmann. 1998. Shape Changes of Self-Assembled Actin Bilayer Composite Membranes. *Physical Review Letters*. 80:1786–1789.

[61] Mauroy, C., T. Portet, M. Winterhalder, E. Bellard, M.-C. Blache, J. Teissié, A. Zumbusch, and M.-P. Rols. 2012. Giant lipid vesicles under electric field pulses assessed by non invasive imaging. *Bioelectrochemistry*. 87:253–259.

[62] Hochmuth, F. M., J. Y. Shao, J. Dai, and M. P. Sheetz. 1996. Deformation and flow of membrane into tethers extracted from neuronal growth cones. *Biophysical Journal*. 70:358–369.

[63] Tolstykh, G. P., G. L. Thompson, H. T. Beier, Z. A. Steelman, and B. L. Ibey. 2017. nsPEF-induced PIP2 depletion, PLC activity and actin cytoskeletal cortex remodeling are responsible for post-exposure cellular swelling and blebbing. *Biochemistry and Biophysics Reports*. 9:36–41.

[64] Pontani, L.-L., J. Van der Gucht, G. Salbreux, J. Heuvingh, J.-F. Joanny, and C. Sykes. 2009. Reconstitution of an actin cortex inside a liposome. *Biophysical journal*. 96:192–198.

[65] Kojima, H., A. Ishijima, and T. Yanagida. 1994. Direct measurement of stiffness of single actin filaments with and without tropomyosin by in vitro nanomanipulation. *Proceedings of the National Academy of Sciences*. 91:12962–12966.

[66] Liu, X., and G. H. Pollack. 2002. Mechanics of f-actin characterized with microfabricated cantilevers. *Biophysical journal*. 83:2705–2715.

[67] Zhang, X., X. Hu, H. Lei, J. Hu, and Y. Zhang. 2016. Mechanical force-induced polymerization and depolymerization of f-actin at water/solid interfaces. *Nanoscale*. 8:6008–6013.

[68] Tsuda, Y., H. Yasutake, A. Ishijima, and T. Yanagida. 1996. Torsional rigidity of single actin filaments and actin–actin bond breaking force under torsion measured directly by in vitro micromanipulation. *Proceedings of the National Academy of Sciences*. 93:12937–12942.

[69] Ott, A., D. Riveline, F. Jülicher, D. WinkelmannD, O. Cardoso, J. Lacapère, S. Magnúsdóttir, J. Viovy, L. Gorre-Talini, and J. Prost. 1999. Acting on actin: The electric motility assay. *Biology of the Cell*. 91:252–252.

[70] Hunt, A. J., F. Gittes, and J. Howard. 1994. The force exerted by a single kinesin molecule against a viscous load. *Biophysical Journal*. 67:766–781.

[71] Retelj, L., G. Pucihar, and D. Miklavčič. 2013. Electroporation of intracellular liposomes using nanosecond electric pulses–a theoretical study. *IEEE Transactions on Biomedical Engineering*. 60:2624–2635.

[72] Rems, L., M. Ušaj, M. Kandušer, M. Reberšek, D. Miklavčič, and G. Pucihar. 2013. Cell electrofusion using nanosecond electric pulses. *Scientific reports*. 3:3382.

[73] DeBruin, K. A., and W. Krassowska. 1999. Modeling electroporation in a single cell. i. effects of field strength and rest potential. *Biophysical journal*. 77:1213–1224.

[74] Chan, K. L., P. R. Gascoyne, F. F. Becker, and R. Pethig. 1997. Electrorotation of liposomes: verification of dielectric multi-shell model for cells. *Biochimica et Biophysica Acta (BBA)-Lipids and Lipid Metabolism*. 1349:182–196.

[75] Haynes, W. M. 2014. CRC handbook of chemistry and physics. CRC press.

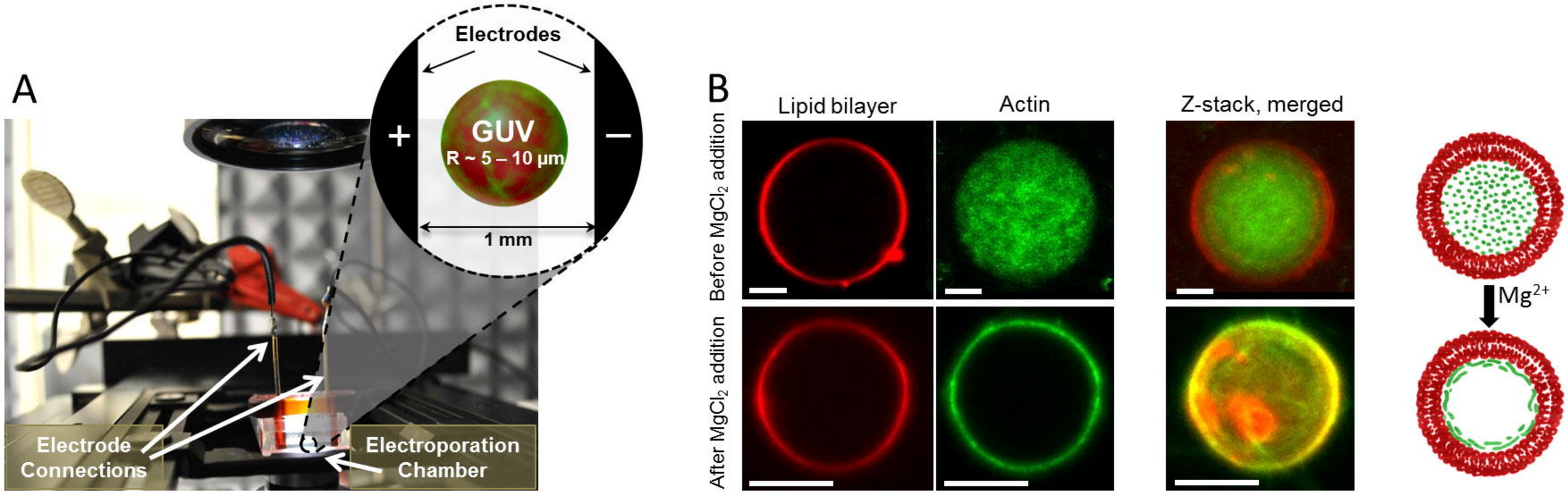
A
Electrodes
+
GUV
R ~ 5 – 10 µm
–
1 mm
Electrode Connections
Electroporation Chamber
B
Lipid bilayer
Actin
Z-stack, merged
Before $MgCl_2$ addition
After $MgCl_2$ addition
Mg^{2+}

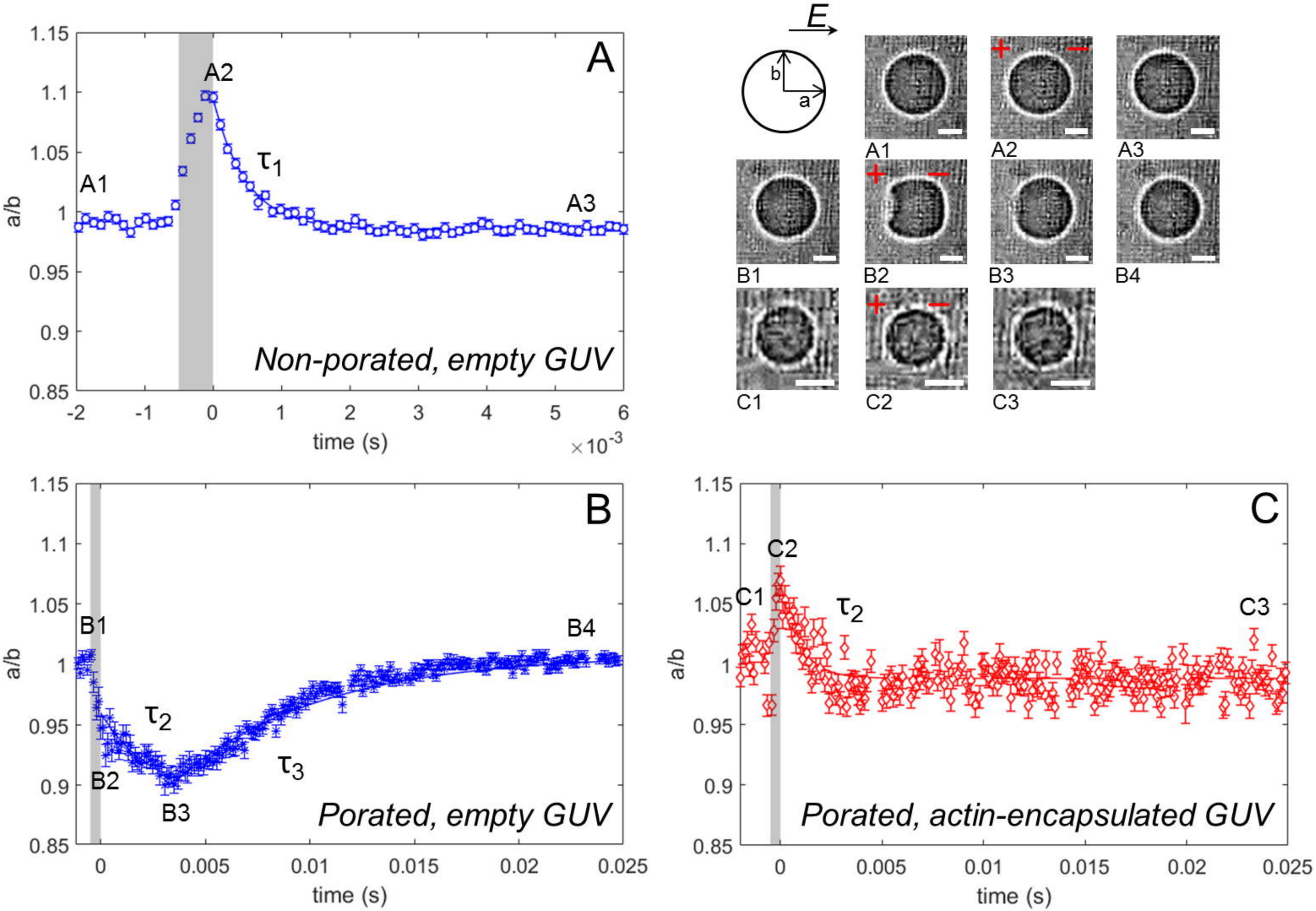
A
A1
A2
A3
τ1
Non-porated, empty GUV
a/b
time (s)
×10^-3
E
b
a
A1
A2
A3
B1
B2
B3
B4
C1
C2
C3
B
B1
B2
B3
B4
τ2
τ3
Porated, empty GUV
a/b
time (s)
C
C1
C2
C3
τ2
Porated, actin-encapsulated GUV
a/b
time (s)

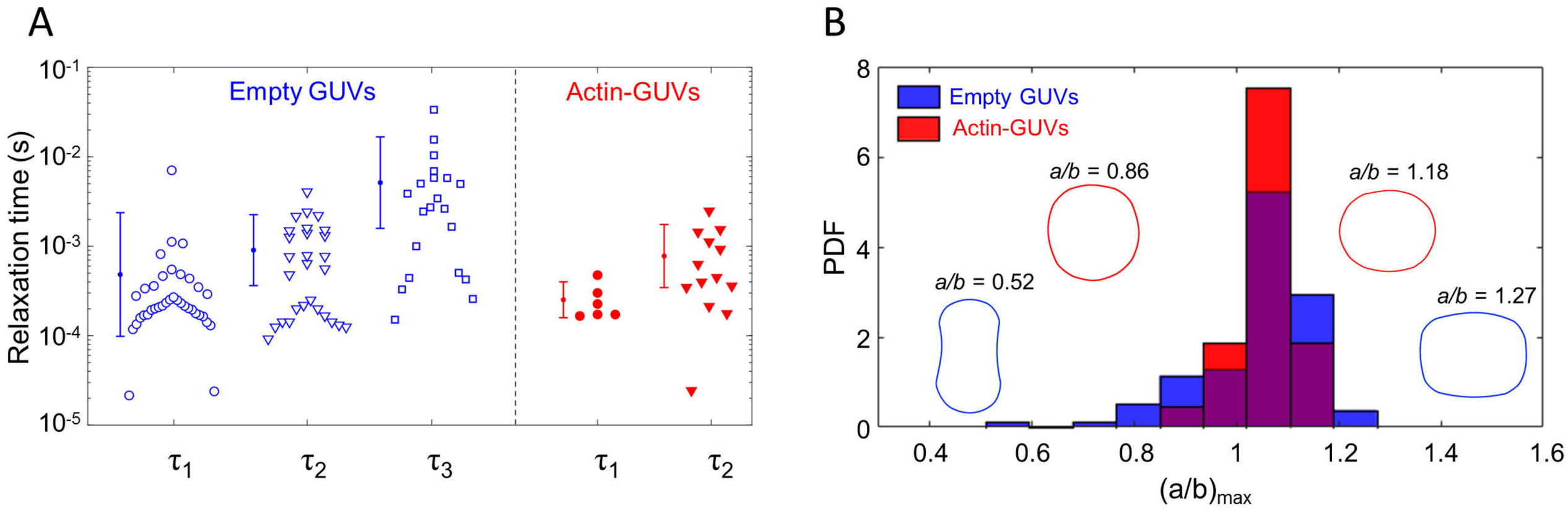
A
Empty GUVs
Actin-GUVs
Relaxation time (s)
10^{-1}
10^{-2}
10^{-3}
10^{-4}
10^{-5}
τ_1
τ_2
τ_3
τ_1
τ_2
B
Empty GUVs
Actin-GUVs
a/b = 0.86
a/b = 1.18
a/b = 0.52
a/b = 1.27
PDF
0
2
4
6
8
0.4
0.6
0.8
1
1.2
1.4
1.6
$(a/b)_{max}$

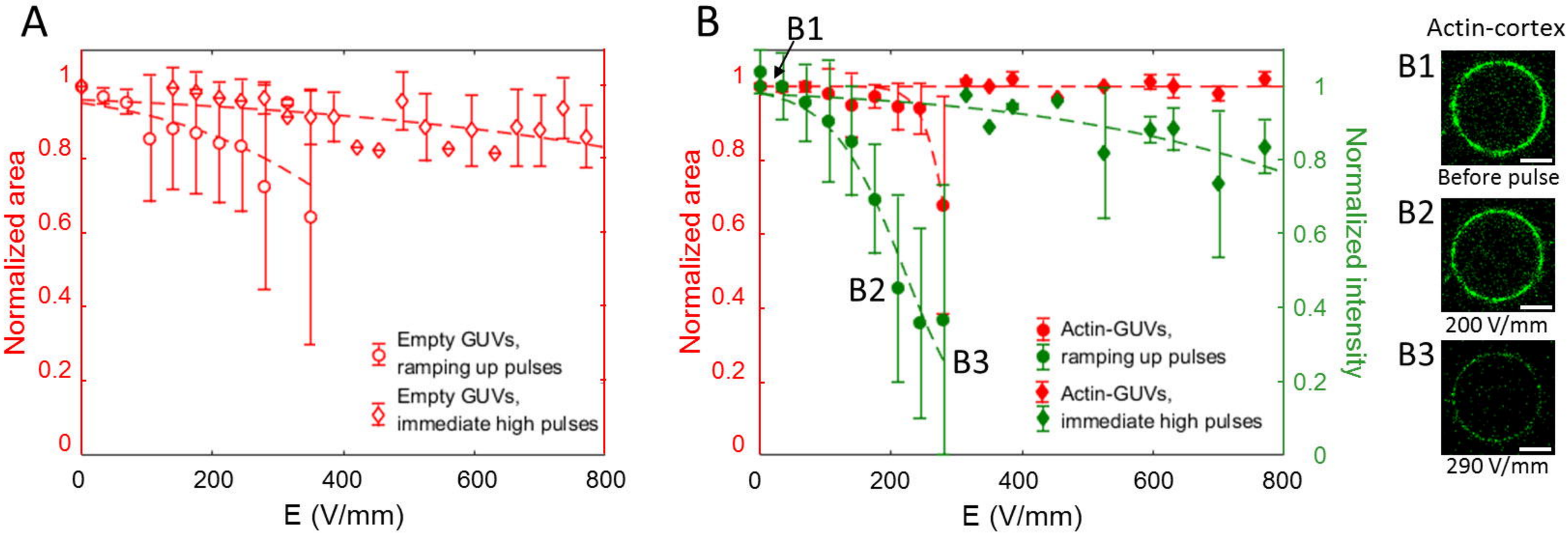
A
Normalized area
E (V/mm)
Empty GUVs, ramping up pulses
Empty GUVs, immediate high pulses
B
B1
B2
B3
Normalized area
Normalized intensity
E (V/mm)
Actin-GUVs, ramping up pulses
Actin-GUVs, immediate high pulses
Actin-cortex
B1
Before pulse
B2
200 V/mm
B3
290 V/mm